

**THEORETICAL INSIGHTS INTO THE TRANSPORT,
KINETICS AND ELECTRONIC PROPERTIES OF
BATTERY MATERIALS FOR ENERGY STORAGE
DEVICES**

DEEPAK SETH



**DEPARTMENT OF CHEMICAL ENGINEERING
INDIAN INSTITUTE OF TECHNOLOGY DELHI
NEW DELHI-110016, INDIA**

JULY 2025

© **Indian Institute of Technology Delhi (IITD), New Delhi, 2025**

**THEORETICAL INSIGHTS INTO THE TRANSPORT,
KINETICS AND ELECTRONIC PROPERTIES OF BATTERY
MATERIALS FOR ENERGY STORAGE DEVICES**

by

Deepak Seth

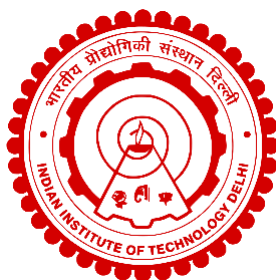
Department of Chemical Engineering

Submitted

in fulfilment of the requirements for the degree of

DOCTOR OF PHILOSOPHY

to the



INDIAN INSTITUTE OF TECHNOLOGY DELHI

JULY 2025

Dedicated to my family and friends....

Certificate

This is to certify that the thesis entitled “**Theoretical Insights into the Transport, Kinetics and Electronic Properties of Battery Materials for Energy Storage Devices**” submitted by **Deepak Seth** to the Indian Institute of Technology Delhi in fulfilment of the requirements for the award of **Doctor of Philosophy** in Chemical Engineering, is a record of bona-fide research work carried out by him. He has worked under our supervision and has fulfilled the requirements, which, to our knowledge, have reached the requisite standard for the submission of the thesis. The research report and results presented in this thesis have not been submitted, in part or full, to any other university or institute for the award of any other degree.



(Prof. M. Ali Haider)

Professor, Department of Chemical Engineering
Indian Institute of Technology Delhi
Hauz Khas, New Delhi-110016,
Vice Provost for Research and External Engagement
Indian Institute of Technology (IIT) Delhi - Abu Dhabi,
Associate Faculty, Yardi School of Artificial Intelligence (ScAI), IIT Delhi



(Dr. Manish Agarwal)

System Manager, CSC
Indian Institute of Technology Delhi
Hauz Khas, New Delhi-110016

Acknowledgements

I feel a wide range of emotions as I wrap up this life-changing Ph.D. journey, including pride, thankfulness, and introspection. This thesis represents much more than just research; it is the culmination of all the highs and lows, struggles and victories, and persistent determinations accumulated over the years.

First and foremost, I want to sincerely thank my supervisors, Prof. M. Ali Haider and Dr. Manish Agarwal. Your unwavering advice, critiques, and encouragement have greatly influenced my academic and professional career direction. I will always have the skills I learned under your guidance in density functional theory (DFT), molecular dynamics (MD), high-performance supercomputing (HPC), etc. I want to express my gratitude to the department's PhD committee members for your insightful advice.

To my colleagues at the REC Lab: thank you for your unwavering support throughout this journey. Chaitra, you were not only my first lab partner at IIT Delhi but also my first friend here, you always had my back, and I am truly grateful. To Jayendran, Ussama, Ashutosh, Iqra, Adarsh, Haseena ma'am, the senior members, and all other lab mates, thank you for your constant encouragement and support. Your contributions helped foster a collaborative and motivating environment that made this journey far less isolating and much more rewarding. The direction of my work was significantly shaped by your advice and support during my time in the lab. From my first year to my last, all of my friends at IIT Delhi helped to make this journey one of support, friendship and shared memories. Every day was brightened by your presence, regardless of the successes and setbacks.

My family has been my strongest asset, above all else. A simple 'thank you' feels insufficient to express my gratitude, but thank you so much to my mother, father, sister, brother, and sister-in-law for always being there for me and everything you have done. In this Ph.D. journey, my wife supported me a lot. I met her in the last year of this journey. Her love,

patience, and faith in me have been a source of immense support throughout this journey. My compass has been your selfless love, support, and sacrifices, which constantly remind me of the principles that have carried me this far.

There have been times of self-doubt and resilience along this journey, which has not been easy. However, each obstacle has strengthened my resolve to reach this goal. I dedicate this work to everyone who has contributed to this journey, no matter how small. I hold your contribution close to my heart.

A handwritten signature in black ink that reads "Deepak Seth". The signature is written in a cursive style with a horizontal line underneath the name.

Deepak Seth

Abstract

Advancements in technologies have led to a significant increase in energy demand, driving the need for efficient energy storage solutions. Energy storage systems such as rechargeable batteries, like lithium-ion (LIBs), sodium-ion (SIBs), and metal-air batteries (MABs), have emerged as promising candidates for energy storage due to their high energy density, long life cycle, and low cost. However, further design strategies in battery materials, including electrodes and/or electrolytes, are required to enhance their electrochemical performance.

The current study focuses on the mechanistic design of various classes of materials for energy storage systems, including aqueous metal-ion batteries, metal-air batteries, and two-dimensional (2D) materials based next-generation energy storage systems. The main objective is to tailor the battery materials and to understand the relationship between ion transport, reaction kinetics, electronic properties and their influence on electrochemical performance, using computational approaches such as density functional theory (DFT) and molecular dynamics (MD) simulations. For aqueous metal-ion batteries, the sodium superionic (NASICON)-structured $ATi_2(PO_4)_3$ ($A=Na, Li$) material is investigated as a potential anode in mixed electrolyte systems containing both Li^+ and Na^+ ions. MD simulations are employed to study and compare the transport properties and energetics of the Na^+ and Li^+ ions in this material. A design strategy involving lattice strain is proposed to enhance Na-ion transport properties. Additionally, the effect of grain boundaries (GB) on Na-ion conductivity and transport properties is explored using various GB structures. For metal-air batteries, the focus is on investigating the kinetic properties of electrocatalyst materials for Zn-air batteries. The performance of Zn-air batteries is limited by the sluggish kinetics of oxygen reduction reaction (ORR) and oxygen evolution reaction (OER) at the air cathode. Molecular-level electronic structure engineering of Co_3O_4 electrocatalysts is explored to

enhance their electrocatalytic activity. The influence of factors such as the concentration of Cu-doped elements on active crystal planes, surface adsorbed intermediates, and electronic structure of the transition metal on the catalytic activity is investigated. For 2D materials, integration of reduced graphene oxide (rGO), including MoS₂ and BFO (BiFeO₃, Bi₂Fe₄O₉, and Bi₂₅FeO₄₀) are investigated for next-generation energy storage devices. Na-ion intercalation properties are studied in MoS₂@rGO and exhibit improved electrochemical performance due to enhanced Na-ion transport, including a reduction in the activation barrier and a corresponding increase in Na-ion diffusivity. BFO@rGO composites demonstrated enhanced electronic and photocatalytic properties, as evidenced by decreased bandgap, attributed to heteroatom (N, S) doped rGO integration.

Overall, the focus of this dissertation is to design novel battery materials for energy storage systems by tuning their ion transport, reaction kinetics, and electronic properties using computational modelling and simulations. The study aims to elucidate the relationship between the modelled structure, composition, material design strategies, and the electrochemical performance of the materials, which can be correlated with experimental observations.

सार

तकनीकी प्रगति ने ऊर्जा की मांग में महत्वपूर्ण वृद्धि की है, जिससे कुशल ऊर्जा भंडारण समाधान की आवश्यकता बढ़ गई है। ऊर्जा भंडारण प्रणालियां, जैसे रिचार्जबल बैटरियां (लिथियम-आयन बैटरियां [LIBs], सोडियम-आयन बैटरियां [SIBs], और मेटल-एयर बैटरियां [MABs]) ऊर्जा भंडारण के लिए आशाजनक विकल्प के रूप में उभरी हैं, क्योंकि इनमें उच्च ऊर्जा घनत्व, लंबा जीवन चक्र, और कम लागत जैसे गुण मौजूद हैं। हालांकि, बैटरी सामग्रियों, जैसे इलेक्ट्रोड और/या इलेक्ट्रोलाइट्स, के डिज़ाइन में और अधिक रणनीतियां विकसित करने की आवश्यकता है ताकि उनकी इलेक्ट्रोकेमिकल प्रदर्शन क्षमता को बढ़ाया जा सके।

वर्तमान अध्ययन विभिन्न ऊर्जा भंडारण प्रणालियों के लिए तीन प्रकार की सामग्रियों के यांत्रिक डिज़ाइन पर केंद्रित है: जलीय मेटल-आयन बैटरियां, मेटल-एयर बैटरियां, और अगली पीढ़ी के ऊर्जा भंडारण उपकरणों के लिए द्वि-आयामी (2D) सामग्री। मुख्य उद्देश्य बैटरी सामग्रियों को अनुकूलित करना और आयन परिवहन, प्रतिक्रिया गतिशीलता, और इलेक्ट्रॉनिक गुणों को इलेक्ट्रोकेमिकल प्रदर्शन से जोड़ने की प्रक्रिया को समझना है, जिसके लिए घनत्व कार्यात्मक सिद्धांत (DFT) और आणविक गतिशीलता (MD) सिमुलेशन जैसे कम्प्यूटेशनल दृष्टिकोणों का उपयोग किया गया है। जलीय मेटल-आयन बैटरियों के लिए, सोडियम सुपरआयोनिक (NASICON) संरचित $ATi_2(PO_4)_3$ ($A=Na, Li$) सामग्री का अध्ययन मिश्रित इलेक्ट्रोलाइट प्रणालियों में संभावित एनोड के रूप में किया गया है, जिनमें Li^+ और Na^+ आयन दोनों शामिल हैं। इस सामग्री में Na^+ और Li^+ -आयनों के परिवहन गुणों और ऊर्जा स्तरों का अध्ययन और तुलना करने के लिए MD सिमुलेशन का उपयोग किया गया है। Na -आयन परिवहन गुणों को बढ़ाने के लिए लैटिस तनाव के उपयोग की रणनीति प्रस्तावित की गई है। इसके अतिरिक्त, Na -आयन चालकता और परिवहन गुणों पर ग्रेन बाउंड्री (GB) के प्रभाव का अध्ययन विभिन्न GB संरचनाओं का उपयोग करके किया गया है। मेटल-एयर बैटरियों के लिए, अध्ययन का मुख्य ध्यान जिंक-एयर बैटरियों में इलेक्ट्रोकेटलिस्ट सामग्रियों के गतिशील गुणों की जांच पर है। जिंक-एयर बैटरियों का प्रदर्शन वायु कैथोड पर ऑक्सीजन रिडक्शन रिएक्शन (ORR) और ऑक्सीजन एवोल्यूशन रिएक्शन (OER) की धीमी गतिशीलता के कारण सीमित है। Co_3O_4 इलेक्ट्रोकेटलिस्ट्स की इलेक्ट्रोकेटलिटिक गतिविधि को बढ़ाने के लिए आणविक स्तर पर इलेक्ट्रॉनिक संरचना इंजीनियरिंग का अध्ययन किया गया है। सक्रिय क्रिस्टल प्लेनों पर Cu -डॉप तत्वों की सांद्रता, सतह पर अवशोषित इंटरमीडिएट्स, और संक्रमण धातु की इलेक्ट्रॉनिक संरचना जैसे कारकों के प्रभाव का विश्लेषण किया गया है। 2D सामग्रियों के लिए, अगली पीढ़ी के ऊर्जा भंडारण उपकरणों के लिए MoS_2 और BFO ($BiFeO_3$, $Bi_2Fe_4O_9$, और

Bi₂₅FeO₄₀) सहित रिड्यूस्ड ग्राफीन ऑक्साइड (rGO) के एकीकरण का अध्ययन किया गया है। MoS₂@rGO में Na-आयन इंटरकलेशन गुणों का अध्ययन किया गया है, जिसमें Na-आयन परिवहन में सुधार, सक्रियण अवरोध में कमी, और Na⁺-आयन के प्रसार में वृद्धि देखी गई है। वहीं, BFO@rGO समग्र सामग्री ने rGO एकीकरण और हेटरोटॉम डोपिंग के कारण इलेक्ट्रॉनिक और फोटोकैटलिटिक गुणों में सुधार दिखाया है, जिसमें बैंडगैप में कमी देखी गई।

कुल मिलाकर, इस शोध का मुख्य उद्देश्य कम्प्यूटेशनल मॉडलिंग और सिमुलेशन का उपयोग करके ऊर्जा भंडारण अनुप्रयोगों के लिए नवीन बैटरी सामग्रियों को डिजाइन करना है। यह अध्ययन मॉडल संरचना, संरचना और सामग्रियों के इलेक्ट्रोकेमिकल प्रदर्शन के बीच संबंध को स्पष्ट करने का प्रयास करता है, जिसे प्रयोगात्मक अवलोकनों से जोड़ा जा सकता है।

Table of Contents

Certificate	i
Acknowledgement	ii
Abstract	iv
Table of Contents	viii
List of Figures	xii
List of Tables	xix
Chapter 1	1
Introduction	1
1.1 Rechargeable batteries.....	2
1.2 Materials for energy storage devices.....	4
1.3 Battery materials	8
1.3.1 NASICONs.....	8
1.3.2 Cobalt oxide (Co ₃ O ₄).....	9
1.3.3 Two-dimensional (2D) materials.....	10
1.3.4 Bi _x Fe _y O _z (BFO)	13
1.4 Materials classifications based on energy storage systems	14
1.5 Materials properties.....	18
1.6 Computational design strategies for the materials	22
1.7 Materials of focus: Linking structure, properties, and electrochemical performance....	24
1.8 Objectives of the thesis	30
Thesis organization	31
Chapter 2	32
Battery materials for energy storage devices: A review	32
2.1 Development of battery materials	32
2.2 Prior research.....	34
2.2.1 NASICONs.....	34
2.2.2 Spinel/metal oxides	40
2.2.2.(b) Co ₃ O ₄	42

2.3 Graphene and its derived two-dimensional (2D) materials	53
2.3.1 MoS ₂	62
2.4 Bi _x Fe _y O _z (BFO)	69
Chapter 3	72
Methods for molecular simulations	72
3.1 Introduction to Molecular Dynamics (MD)	72
3.1.1 Potential energy functions	73
3.1.2 Boundary conditions	75
3.1.3 Thermostat and barostat	77
3.1.4 Ensemble	77
3.1.5 Equilibration and production runs	78
3.1.6 Post-simulation analysis of MD	78
3.2 Introduction to density functional theory (DFT)	80
3.2.1 Fundamental theorems of DFT	82
3.2.2 DFT calculations (self-consistency field)	85
3.3 Lattice strain effect	86
3.4 Grain boundary	87
GB classical models	88
Classifications of GB:	89
Coincidence site lattice (CSL) grain boundary	90
Grain boundary energies	91
Grain boundary effects on material properties	92
Chapter 4	94
Na-ion transport in NASICON structured NaTi₂(PO₄)₃ for SIBs	94
4.1 Introduction	94
4.2 Computational method	97
4.3 Results and discussion	100
4.4 Summary	118
Chapter 5	120

Mixed (Na⁺/Li⁺)-ions transport in NaTi₂(PO₄)₃ for SIBs	120
5.1 Introduction	120
5.2 Computational method	122
5.3 Results and discussion.....	123
5.4 Summary	138
Chapter 6	139
Electrocatalytic properties of Cu-doped Co₃O₄ material for metal-air battery	139
6.1 Introduction	139
6.2 Computational method	141
6.3 Results and discussion.....	145
6.4 Summary	155
Chapter 7	156
Design of 2D materials for energy storage devices	156
7A Understanding Na-ion intercalation in metal-doped MoS₂@rGO for SIBs	157
7A.1 Introduction	157
7A.2 Computational method	160
7A.3 Results and discussion.....	161
7A.4 Summary	174
7B Study of heteroatoms (N, S-)-doped Bi_xFe_yO_z (BFO)@rGO as efficient photoanode	176
7B.1 Introduction	176
7B.2 Computational method	177
7B.3 Results and discussion.....	178
7B.4 Summary.....	184
Chapter 8	185
Conclusions and future outlook.....	185
Bibliography	188
Appendix A.....	208
Appendix B.....	219

Appendix C	222
Appendix D	227
Publications related to this thesis	230
Journal papers.....	230
Conference papers	230
Copyright permissions from journals	231
Biodata	245

List of Figures

Figure 1.1 Schematic of functioning of an electrochemical cell in (a) alkali-ion rechargeable battery (b) Metal (Zn)-air batteries	3
Figure 1.2 Ragone plot comparing energy and power densities of energy storage devices	5
Figure 1.3 Specific capacity and cost comparison (b) Global availability comparison of different alkali-ion battery precursor materials.....	5
Figure 1.4 NASICON-structured type material with R-3c symmetry	9
Figure 1.5 Normal spinel, Co_3O_4 structure with Co^{+2} (green atom) and Co^{+3} (blue atoms) and O atom (red).....	10
Figure 1.6 2D structures of (a) graphene (b) graphene oxide (c) reduced graphene oxide [Color Scheme: C (grey), O (red), H (white)]	11
Figure 1.7 Top view and stacking configurations of MoS_2 structures for the (a) 1T phase, (b) 2H phase, and (c) 3R phase [Color Scheme: S (yellow), Mo (Cyan)].....	12
Figure 1.8 Crystal structure of (a) rhombohedral BiFeO_3 (b) orthorhombic $\text{Bi}_2\text{Fe}_4\text{O}_9$ (c) cubic $\text{Bi}_{25}\text{FeO}_{40}$	13
Figure 1.9 Classification of energy storage systems.....	14
Figure 1.10 Illustrates the mechanism of an aqueous metal-ion rechargeable battery, showing $\text{Li}^+/\text{Na}^+/\text{K}^+/\text{Mg}^{2+}$ ion transport through a water-in-salt electrolyte, with a layered graphite anode (as an example) and a crystalline metal oxide cathode	15
Figure 1.11 Mechanism of ion transport in the solid materials: (a) vacancy diffusion via vacant stable cation sites, (b) interstitial diffusion through metastable cation sites, and (c) correlated diffusion involving cooperative ion movement	19
Figure 1.12 Thermodynamic and kinetic factors in aqueous energy storage systems, illustrating the narrow electrochemically stable voltage window (ESW) of the electrolyte leading to oxygen evolution reaction (OER) at the cathode, and the high energy barrier of conversion reactions at the electrode interfaces.....	21
Figure 1.13 Illustrates the energy level diagram for typical metals, showing the overlapping conduction and valence bands with no bandgap ($eg = 0$) and the Fermi level (E_F) positioned within this overlap, facilitating high electron conductivity.	21
Figure 1.14 Effect of tensile strain in a thin film, showing a thin film-substrate interface with lattice alignment, where arrows indicate the direction of strain-induced in the lattice, influencing the ion movement.	23

Figure 1.15 Schematics of element doping via substitution in the system	24
Figure 1.16 Schematics of the explicit solvent effect on the MnO ₂ surface enhancing the electrocatalytic reaction process: solvent molecules (blue) interacting with the MnO ₂ surface, stabilizing intermediates (e.g., *OOH).	24
Figure 1.17 Materials of focus in the dissertation research	25
Figure 2.1 Comparison of specific energies of rechargeable batteries. [*Reproduce with permission from ref. 91]	33
Figure 2.2 Structure of oxide materials showing (a) normal spinel, (b) inverse spinel (c) complex spinel	41
Figure 2.3 Schematics of proposed ORR mechanism on oxide surface	47
Figure 2.4 Volcano plot determined by utilizing Sabatier analysis showing a correlation between oxygen binding energy (ΔE_O) and peak activity for ORR of different metals. [*Reproduce with permission from ref. 194].....	48
Figure 2.5 (a) Graphene layers (b) single sheet of graphene layer containing carbon atoms in hexagonal lattice arrangements.....	55
Figure 2.6 Illustrates d-orbital occupation and electronic properties of different TMDCs. [*Reproduce with permission from ref. 260].....	64
Figure 2.7 Tuning of material, including interlayer spacing to accommodate large ion	66
Figure 2.8 Schematics of advantages of metal doping in MoS ₂ /rGO system.....	68
Figure 3.1 Plot of Lennard-Jones potential functions (with repulsive and attractive terms)..	73
Figure 3.2 Plot of (a) Buckingham and (b) morse potential functions	74
Figure 3.3 Represents PBC in 2D images for a cubic cell (central cell in light orange color) with velocity vector (by arrow), r_{cut} and short-range interaction within a sphere.	76
Figure 3.4 Electron-Nuclei interaction in N particle system	80
Figure 3.5 Schematics of Born-Oppenheimer approximations.....	81
Figure 3.6 Schematic of second approximations, $\rho(r)$	82
Figure 3.7 Flowchart represents the self-consistency field in Kohn-Sham DFT	83
Figure 3.8 Schematics of polycrystalline materials forming a GB region between grains A & B, B & C, and A & C.....	88
Figure 3.9 Represents spherical angles Θ and ϕ and GB normal plane, n	88
Figure 3.10 Schematics of tilted grain boundary and twisted grain boundary	89

Figure 3.11 Illustrating the formation of $\Sigma 5$ GB for cubic crystal.....91

Figure 4.1 (a) $\text{NaTi}_2(\text{PO}_4)_3$ crystal structure (polyhedral view) with Na-ion vacancy. Na-ion migration along **(b)** [001] **(c)** [010], and **(d)** [100] direction..... 101

Figure 4.2 Represents **(a)** MSD vs time plot for Na-ion in pristine $\text{NaTi}_2(\text{PO}_4)_3$ for three vacancy distributions. Density diagrams depict the trajectory for **(b)** all Na atoms **(c)** a single Na atom, changing from the initial (blue) to the final (green) steps..... 105

Figure 4.3 Temperature-dependent **(a)** MSD plot of Na-ions and **(b)** corresponding Na-ion self-diffusivity in $\text{NaTi}_2(\text{PO}_4)_3$ 106

Figure 4.4 Represents Na-ion diffusion coefficient change over **(a)** biaxial strain and **(b)** uniaxial strain in $\text{NaTi}_2(\text{PO}_4)_3$. **(c)** MSD vs time plot for 0% and 3% strain effect..... 109

Figure 4.5 Activation energy (E_a) corresponds to the biaxial lattice strain structure along [001] direction for xy tensile strain in $\text{NaTi}_2(\text{PO}_4)_3$ 110

Figure 4.6 (a) DFT energies **(b)** Na-ion vacancy formation energies in $\text{NaTi}_2(\text{PO}_4)_3$ biaxial strained structure. 111

Figure 4.7 Grain Boundary, B.1 : $\Sigma 5[001]/(120)$ 112

Figure 4.8 GB energies of all the $\text{NaTi}_2(\text{PO}_4)_3$ GB models 113

Figure 4.9 (a) Na-ion diffusivity **(b)** Corresponding Na-ion ionic-conductivity for both bulk (grain to grain) and grain boundary components of all GB models **(c)** MSD of Na-ion for all GB models at the grain boundary (green line) and at the bulk (blue line)..... 115

Figure 4.10 (a) Na-ion activation energy comparison between GBs **(b)** Na-ion ionic-conductivity vs grain boundary energies for all GB models..... 117

Figure 4.11 Na-ion distribution at GB region with corresponding potential energies..... 118

Figure 5.1 Represents the radial distribution function (RDF) of **(a)** Na-Na, **(b)** Na-O and **(c)** P-O respectively in (Red) compared with the initial data (black) after all NPT-MD steps... 124

Figure 5.2 Fluctuations of lattice parameters **(a)** a (Å) **(b)** b (Å) **(c)** c (Å) **(d)** α (deg.) **(e)** β (deg.) **(f)** γ (deg.) of $\text{NaTi}_2(\text{PO}_4)_3$ for the overall MD simulation of 10 ns using the partial charge pair potential parameters 125

Figure 5.3 (a) Enlarged cation density profile of the mixed-ion structure ($\text{Na}_{x-y}\text{Li}_y\text{Ti}_2(\text{PO}_4)_3$) representing Na (blue) and Li atoms (light pink) along with the framework tetrahedron PO_4 (light green) and octahedron TiO_6 (purple), **(b)** MSD versus time plot of Na^+ (blue) and Li^+ (red) ions in the mixed-ion structure..... 128

Figure 5.4 Density diagrams represent the trajectory visual for all (c) Na atoms (d) Li atoms (changing its state from initial step (in blue) to the final step (in green)), respectively.	129
Figure 5.5 Represents (a) Na ⁺ (blue) and Li ⁺ (pink) mixed-ion structure along with the framework PO ₄ (light green) tetrahedra and FeO ₆ (cyan) octahedra, (b) MSD versus time plot of Na ⁺ (blue) and Li ⁺ (pink) ions in the mixed-ion LiFePO ₄ structure.	131
Figure 5.6 (a) MSD vs time plot for Li-ion for three vacancy distributions in LiTi ₂ (PO ₄) ₃ (b) Density diagrams depict the trajectory for Li atom (changing its state from initial step (in blue) to the final step (in green)).....	132
Figure 5.7 Temperature-dependent (a) MSD plot of Li-ion and (b) corresponding Li-ion self-diffusivity in LiTi ₂ (PO ₄) ₃	133
Figure 5.8 (a) Lattice strain effect on Li-ion diffusion-coefficient over biaxial strain in LiTi ₂ (PO ₄) ₃ (b) MSD vs time plot comparison of Li atoms for all xy lattice strain in LiTi ₂ (PO ₄) ₃ structure (c) Lattice strain effect on Li-ion diffusion-coefficient over uniaxial strain (d) MSD vs time plot for 0% and 3% strain for Li-ion in LiTi ₂ (PO ₄) ₃	135
Figure 5.9 (a) Activation energy (E _{a,Li+}) corresponds to the biaxial lattice strain structure along [001] direction in LiTi ₂ (PO ₄) ₃ . (b) (E _{a,Na+}) and (E _{a,Li+}) comparisons for xy strain.	136
Figure 5.10 (a) DFT energies (b) Li-ion vacancy formation energies, in LiTi ₂ (PO ₄) ₃ biaxial strained structure.	137
Figure 6.1 Density diagrams of Cu atoms for (a) 5% and (b) 20% Cu-doped structures, corresponding to the final frame after all MD simulation steps. In the 20% Cu-doped structure, significant segregation of Cu ions from the bulk and/or sub-layers to the surface is observed, whereas in the 5% Cu-doped structure, the Cu atoms largely remain uniformly distributed and intact within the lattice.	146
Figure 6.2 Cu-atom doped at (a) octahedral site (Cu _{Oh}) (b) tetrahedral site (Cu _{Th}) of Co ₃ O _{4-δ} structure (δ represents the oxygen non-stoichiometry). pDOS of (c) undoped Co ₃ O _{4-δ} (d) Cu _{Th} - Co ₃ O _{4-δ} (e) Cu _{Oh} - Co ₃ O _{4-δ}	147
Figure 6.3 Surface formation energy for different surface slabs	147
Figure 6.4 Represents Co (blue), O (red) and Cu (orange) atom's Bader charge for (a) undoped and (b) doped (311) Co ₃ O _{4-δ} active sites.....	149
Figure 6.5 Cu-doped Co ₃ O _{4-δ} (311) surface with layers of water molecules, showing the adsorbed (a) O (b) OH and (c) OOH, with the corresponding inset (zoomed and rotated) images of adsorbate (hydrogen bonding with the black dash line and hydrogen-bond distance)	

(d) Reaction free energy diagram for ORR at pH=13 for Cu-doped (orange) and undoped (blue) $\text{Co}_3\text{O}_{4-\delta}$ (311) [color scheme: H in white, O in red, Co in blue, and Cu in orange].... 150

Figure 6.6 Potential energy diagram for OER with activation barrier, for Cu-doped (orange) and undoped (blue) $\text{Co}_3\text{O}_{4-\delta}$ (311) surface..... 153

Figure 7.1 (a) Top view of layered Al (in purple) doped 1T-MoS₂ on reduced graphene oxide structure showing Na atoms (in blue) at hollow-hollow site in grey hexagonal block. Mo (cyan) S (yellow) C (black) O (red) H (white). **(b)** Front view of optimized structure of Na-ion in layered Al-doped 1T MoS₂@rGO indicating the migration distance **(c)** the Na-ion migration (blue-white-red) pathways in 1T Al-MoS₂@rGO interlayer..... 164

Figure 7.2 (a) top view and **(b)** front view, of Na-ion hopping in between MoS₂ and rGO layer (configuration 1) 165

Figure 7.3 (a) top view **(b)** front view, of Na-ion hopping at above MoS₂/rGO layer (configuration 2) 165

Figure 7.4 Doping of TM atoms (green color) with Mo (yellow) and Na-ion (blue) hopping in **(a)** C_I (M₁ – C₁ – M₂) **(b)** C_{II} (M₁ – C₂ – M₂)..... 167

Figure 7.5 (a) DFT energies **(b)** Change in the energy w.r.t to undoped system 168

Figure 7.6 Projected density of states (PDOS) plots for **(a)** C_I and **(b)** C_{II} with (a.1, b.1) for Sc and (a.2, b.2) for Ti doping. 169

Figure 7.7 Represents the d-band center shift for **(a)** C_I and **(b)** C_{II} 171

Figure 7.8 Interfacial Na-ion binding energies in **(a)** C_I and **(b)** C_{II}..... 172

Figure 7.9 Energy profile of Na-ion diffusion path for **(a)** C_I and **(c)** C_{II} and corresponding activation energy (E_a) for all dopants for **(b)** C_I and **(d)** C_{II} 174

figure 7.10 Representing front view (1) and top view (2), **(a)** BiFeO₃@undoped rGO **(b)** Bi₂Fe₄O₉@N-doped rGO **(c)** Bi₂Fe₄O₉@S-doped rGO and **(d)** Bi₂₅FeO₄₀@N,S-co-doped rGO. [Color Scheme: O in red, Bi in light pink, Fe in cyan, C in grey, N in blue, S in yellow, and H in white]..... 180

Figure 7.11 Band structure and DOS plots for all atoms in **(a)** BiFeO₃@undoped rGO **(b)** Bi₂Fe₄O₉@N-doped rGO **(c)** Bi₂Fe₄O₉@S-doped rGO, and **(d)** Bi₂₅FeO₄₀@N,S-co-doped rGO. 181

Figure 7.12 Projected DOS plots for all atoms in **(a)** BiFeO₃@undoped rGO **(b)** Bi₂Fe₄O₉@N-doped rGO **(c)** Bi₂Fe₄O₉@S-doped rGO, and **(d)** Bi₂₅FeO₄₀@N,S-co-doped rGO. 182

Figure A.1 NaTi ₂ (PO ₄) ₃ structure with Na-ion position	188
Figure A.2 pDOS of all atoms for (a.1) pristine NaTi ₂ (PO ₄) ₃ (a.2) a Na-ion vacant NaTi ₂ (PO ₄) ₃ (b.1) pristine LiTi ₂ (PO ₄) ₃ (b.2) a Li-ion vacant LiTi ₂ (PO ₄) ₃	190
Figure A.3 Na-ion self-diffusion coefficient and corresponding Na-ion conductivity in x, y and z directions of NaTi ₂ (PO ₄) ₃ crystal.....	191
Figure A.4 Temperature-dependent lattice change in NaTi ₂ (PO ₄) ₃ for (a) cell parameter, “c” (b) cell parameter, “a”	192
Figure A.5 Uniform cell volume change with strain effect for both uniaxial and biaxial directions.....	192
Figure A.6.(a) Grain Boundary, A : $\Sigma 3[111]/(1-21)$	193
Figure A.6.(b) Grain Boundary, B.1 : $\Sigma 5[001]/(120)$	194
Figure A.6.(c) Grain Boundary, B.2 : $\Sigma 5[001]/(2-10)$	194
Figure A.6.(d) Grain Boundary, B.3 : $\Sigma 5[001]/(130)$	195
Figure A.6.(e) Grain Boundary, B.4 : $\Sigma 5[010]/(201)$	196
Figure A.6.(f) Grain Boundary, B.5 : $\Sigma 5[100]/(012)$	196
Figure A.6.(g) Grain Boundary, C : $\Sigma 11[110]/(120)$	196
Figure A.6.(h) Grain Boundary, D.1 : $\Sigma 13[001]/(230)$	197
Figure A.6.(i) Grain Boundary, D.2 : $\Sigma 13[001]/(001)$	198
Figure A.7 Schematic representation of (a) uniaxial tensile strain and (b) biaxial lattice strain, applied to the NaTi ₂ (PO ₄) ₃ and LiTi ₂ (PO ₄) ₃ crystal lattices, showing the elongation of lattice deformation, as used in this study.....	198
Figure B.1 Represents MSD vs time plot for (a) 10% (b) 20% and (c) 30 % Na-ion vacancy for large supercell, respectively (d) combined images of (a), (b) and (c).	200
Figure B.2 pDOS of all atoms in strained (a) NaTi ₂ (PO ₄) ₃ and (b) LiTi ₂ (PO ₄) ₃ crystal structures.....	201
Figure C.1 Energy minimized Co ₃ O _{4-δ} (311) surface representing (a) three possible Co site (yellow color) (b) the fixed atoms (white color) (c) without Cu doping (d) with Cu doping.	202

Figure C.2 (a) Illustrates the transfer of H onto the Cu-Co ₃ O ₄ surface [numbers 1 to 8 represent the neb images of the simulations] (b) Energies of intermediate neb images of the H transfer process on the MEP with a barrier of 0.09 eV	205
Figure C.3 Oxygen evolution reaction mechanism pathways for all elementary steps	206
Figure D.1 Projected density of states (PDOS) plots in configuration 1 (C _I) for (a) V (b) Cr (c) Mn (d) Fe (e) Co (f) Ni (g) Cu and (h) Zn, doping	207
Figure D.2 Projected density of states (PDOS) plots in configuration 2 (C _{II}) for (a) V (b) Cr (c) Mn (d) Fe (e) Co (f) Ni (g) Cu and (h) Zn, doping	207
Figure D.3 FESEM images of (a) G/BFO, (b) NG/BFO using N-doped graphene oxides nanosheets (N-GNS), (c) SG/BFO using S-doped graphene oxide nanosheets (S-GNS) and (d) NSG/BFO using (N, S)-co-doped graphene oxide nanosheets (NS-GNS) heterostructures	209

List of Tables

Table 1.1 List of different kinds of materials for energy storage devices.....	6
Table 2.1 Diffusion coefficient comparison in NASICONs-based materials	36
Table 2.2 Graphene-driven advanced features in energy storage devices	59
Table 2.3 Electronic properties of various TMDCs	63
Table 5.1 Comparison of lattice parameters of crystal primitive cell after all NPT-MD steps	125
Table 5.2 Diffusion-coefficient values of Na-ion and Li-ion in a (Na ⁺ /Li ⁺) mixed-ion NaTi ₂ (PO ₄) ₃ structure.....	129
Table 5.3 Diffusion-coefficient values of Na-ion and Li-ion in a (Na ⁺ /Li ⁺) mixed-ion LiFePO ₄ system	131
Table 6.1 Enthalpy change and TS for all OER steps.....	154
Table 7.1 Na-ion activation energy values with the migration distances.....	163
Table 7.2 Comparison and analysis of PDOS results for all the TMs dopants suitable for energy storage devices	169
Table 7.3 Comparisons of bandgap, E _g (eV) values for structures with and without defects	184
Table A.1 Pair-potential parameters applied in this work.....	188
Table A.2 Vacancy formation energy for inside four Na sites in bulk solid NaTi ₂ (PO ₄) ₃ crystal.....	189
Table A.3 Na-ion activation energy along different directions in bulk solid NaTi ₂ (PO ₄) ₃ crystal.....	189
Table A.4 Average self-diffusion coefficient values of Na-ion along x, y and z direction in bulk Na _x Ti ₂ (PO ₄)	191
Table A.5 Ionic conductivity comparisons for GB region and its bulk	193
Table B.1 Pair-potential parameters of Pedone et al. applied in this work.....	199
Table B.2 Na-ion diffusion coefficient values corresponding to various concentrations of Na-ion.	199
Table B.3 Average self-diffusion coefficient values of Li-ion along x, y and z direction in bulk Na _{x-y} Li _y Ti ₂ (PO ₄)	201
Table B.4 Comparison of lattice parameters of NaTi ₂ (PO ₄) ₃ after geometry optimization using DFT	201
Table C.1 Zero-point energy (ZPE) and TS values of reference and adsorbed molecule	203
Table C.2 Pair-potential parameters applied in this work for Cu segregations	204
Table C.3 Cu doped surface energies at different Co sites	204

Table C.4 Comparison of lattice parameters of Co_3O_4 after geometry optimization using DFT204

Table D.1 Comparison of lattice parameters of 1T- MoS_2 bulk layer after geometry optimization using DFT208